Akbari Rahimabadi, Ahmad, Kerfriden, Pierre and Bordas, Stephane 2015. Scale selection in nonlinear fracture mechanics of heterogeneous materials. Philosophical Magazine 95 (28-30) , pp. 3328-3347. 10.1080/14786435.2015.1061716

Publishers page: http://dx.doi.org/10.1080/14786435.2015.1061716

Philosophical Magazine
Vol. 00, No. 00, 00 Month 2015, 1–21

RESEARCH ARTICLE

Scale selection in nonlinear fracture mechanics of heterogeneous materials

Ahmad Akbari R.[a,b] , Pierre Kerfriden [a*] and Stéphane Bordas [a,c]
[a] *Cardiff University, School of Engineering, Queen's Buildings, The Parade, Cardiff CF24 3AA, Wales, UK*;

[b] *Department of Mechanical Engineering, Kermanshah branch, Islamic Azad University, Kermanshah, Iran*;

[c] *Research Unit in Engineering Science, Luxembourg University, 6 rue Richard Coudenhove-Kalergi, L-1359 Luxembourg, Luxembourg*

(*Received 00 Month 200x; final version received 00 Month 200x*)

A new adaptive multiscale method for the nonlinear fracture simulation of heterogeneous materials is proposed. The two major sources of error in the finite element simulation are discretisation and modelling errors. In the failure problems, the discretisation error increases due to the strain localisation which is also a source for the error in the homogenisation of the underlying micro-structure. In this paper, the discretisation error is controlled by an adaptive mesh refinement procedure following the Zienkiewicz-Zhu technique, and the modelling error, which is the resultant of homogenisation of micro-structure, is controlled by replacing the macroscopic model with the underlying heterogeneous micro-structure. The scale adaptation criterion which is based on an error indicator for homogenisation proposed by[1] is employed for our nonlinear fracture problem. The control of both discretisation and homogenisation errors is the main feature of the proposed multiscale method.

Keywords: Multiscale, Fracture, adaptive mesh, homogenisation error, discretisation error.

1. Introduction

Computational homogenisation and multiscale domain decomposition methods are two distinct approach to simulate fracture mechanics whilst taking into account the microstructure of the material. In computational homogenisation methods [2–7], the macroscopic constitutive relations are implicitly defined by linking the macroscopic material point to the Representative Volume Element (RVE). Incremental macroscopic stress-strain relationships are obtained "on-the-fly" during the macroscopic solution process by solving the boundary value problem associated with the RVE at each (quadrature) point of the macroscopic problem. Such hierarchical multiscale methods rely on the theory of homogenisation [8–12], and assume the existence of a clear separation of scale. Indeed, homogenisation methods share similarities with many other upscaling multiscale methods. The main idea of upscaling techniques is to form a coarse-scale equation and pre-compute the effective coefficients. For example, in Multiscale Finite Element Method (MsFEM), the fine scale information is upscaled to the coarse scale through the coupling of the global

---

*Corresponding author. Email: pierre.kerfriden@gmail.com

ISSN: 1478-6435 print/ISSN 1478-6443 online

DOI: 10.1080/14786435.20xx.xxxxxx
http://www.informaworld.com

stiffness matrix [13]. However, the convergence of the MsFEM suffers from resonance effects when the size of coarse mesh h is of the same order of magnitude as the microscopic characteristic length scale ϵ and the classical finite element method does not converge if $h \gg \epsilon$ [14].

In general, these methods fail to represent correctly the behaviour of the structure in highly strained regions due to the violation of this assumption, although modern higher-order homogenisation schemes can accommodate moderately large macroscopic deformations (see for instance [15, 16]). In the case of fracture mechanics, hierarchical multiscale methods cannot be used in a straightforward manner in the vicinity of cracks, as the separation of scales necessary for their application is lost due to highly localised strain gradients. Crack tip properties in a heterogeneous structure cannot be accurately determined by replacing the whole structure with a homogenised medium and calculating the SIF of the crack in that medium. For example, [17] proposed that the crack tip region must explicitly be retained with the actual micro-structure, and at best replace the surrounding region with the homogenised medium.

Concurrent multiscale schemes can be employed in order to alleviate the absence of the scale separation assumption. These methods make use of a domain decomposition framework whereby the zones where homogenisation fails are directly modelled at the microscale (e.g. [18–23]).In the context of fracture mechanics, concurrent multiscale methods take advantage of the fact that only a small portion of the total domain is affected by high strain concentrations [24, 25]. Both scales (or all scales) are resolved simultaneously. Information is exchanged between the scales through the interfaces of the domain decomposition. In order to represent crack propagation, the microscale domain needs to be adaptively expanded into new critical regions [19, 20, 26]. In such a failure-oriented concurrent multiscale method, the main challenges are to

- adequately model the coupling between the scales,
- determine those regions which must be modelled at the microscale and those for which a macroscale model is sufficient,

To tackle the first challenge, several coupling techniques have been proposed in the literature. Overlapping domain decomposition techniques are usually preferred when the physics at the different scales involved have incompatible kinematics (e.g. atomistic versus continuum), for instance in the context of the Arlequin framework [27], whilst non-overlapping domain decomposition framework are usually used to couple macroscopic homogeneous and microscopic heterogeneous continua, for instance the Mortar Element method [28, 29], or the Linear Multi-Point Constraint approach (or strong coupling) [20]. The latter will be employed in this paper. [19] investigated three different coupling methods between coarse and fine scales, both modelled using continuum mechanics: the Mortar method which connects fine and coarse meshes in an average sense and over an interface between two non-overlapping domains; the Arlequin method which connects two overlapping domains; and the strong coupling method which provides a strong connection between the displacement fields of the fine and coarse meshes over their interface, in a non-overlapping fashion.

To overcome the second challenge, several criteria have been proposed in order to determine the adequate modelling scale in the failure-oriented concurrent multiscale methods. These criteria are mostly based on the local state of the material (for example based on the level of damage, stress or strain [20, 30]). On the other hand, in the context of linear or mildly nonlinear multiscale problems, a number of contributions have proposed to drive the scale adaptivity using modelling error estimates (indicators of a distance between the macroscopic response and the unknown response of the underlying microscopic structure) [1, 31–35]. Oden and Zohdi [36] developed an adaptive concurrent multiscale method for linear elastic problem with a posteriori error estimator for homogenisation. In [37], the theory of a posteriori modelling error estimation for heterogeneous materials was extended to local features of the response, for example, average stresses on material interfaces, boundary displacements, or pointwise displacements, strains, or stresses. Romkes and Oden [38] presented an extension of the goal oriented estimation to the elastodynamic problem. [39] devised an adaptive multiscale method by using a posteriori error estimation and implementing the method for three-dimensional systems involving molecular models, continuum models, and hybrid models. [40] improved [41] by proposing a method that optimally determines the critical area in continuum model to couple with atomistic scale with respect to the quantities of interest. However, none of the concurrent multiscale methods for fracture mechanics have employed the modelling error as scale adaptation criterion.

The first aim of this paper is to expose an hybrid multiscale method, which is a combination of both the homogenisation and the domain decomposition approaches. This new approach will be developed for the simulation of fracture in polycrystalline materials. The second aim of this paper is to select an adequate scale selection criterion based on the ideas of modelling error control. Zohdi et al. [42] proposed a domain decomposition method where the large micro-scale problem is decoupled into several sub-domains. An error estimation technique based on the Principle of Minimum Potential Energy (PMPE) was developed in which the errors of coarse scale discretisation, fine scale discretisation and the decoupling error can be determined. They also derived an error bound for their error estimator. In a special case, the error bound for the domain decomposition problem reduces to bounds on effective material properties which was proved to be identical to the Reuss-Voigt inequalities. The work was an extension to their previous paper [31] in which the fine scale discretisation error was ignored. The natural error between the exact solution $\mathbf{u}$ and the coarsest scale solution $\mathbf{u}^{(0,h)}$ is defined by [43, 44]:

$$\|\mathbf{u}-\mathbf{u}^{0,h}\|_{E(\Omega)} \leq \underbrace{\|\mathbf{u}-\mathbf{u}^{0}\|_{E(\Omega)}}_{\text{modelling error}} + \underbrace{\|\mathbf{u}^{0}-\mathbf{u}^{0,h}\|_{E(\Omega)}}_{\text{Numerical error}}. \tag{1}$$

where h is the size of coarse scale mesh, and the superscript 0 indicates the homogeneous (regularized) solution. Zohdi et al [45] developed an error bound for the regularized solution of an inhomogeneous domain:

$$\|\mathbf{u}-\mathbf{u}^{0}\|^{2}_{E(\Omega)} \leq \int_{\Omega} ((\mathbb{R}-\mathbb{E}):\nabla\mathbf{u}^{0}):\mathbb{E}^{-1}:((\mathbb{R}-\mathbb{E}):\nabla\mathbf{u}^{0})d\Omega \tag{2}$$

Where $\mathbf{u}$ and $\mathbf{u}^0$ are the primal solution for inhomogeneous and regularized (homogenized) domain respectively. $\mathbb{R}$ is the elasticity tensor of regularized domain, and $\mathbb{E}(\mathbf{x})$ is the elasticity tensor of inhomogeneous domain. Even though, this error bound does not require a complex microscale simulation, it is required to map the elasticity of inhomogeneous domain to the coarse scale coordinate system which is not always possible in engineering problems. In addition, their work is limited to linear cases and small problems as one needs to mesh the microstructure and compute the fine scale homogenised solution.

The micro elasticity problem includes damage evolution at grain interfaces which cannot be taken into account by the error bound given in [45]. Hence, the proposed error bound for homogenisation gives an larger band for the modelling error in microstructures with discontinuities since it is incapable of considering material degradation happening at grain interfaces in inhomogeneous domains.

Similarly, the error in the homogenized solution can be introduced by:

$$\|\mathbf{u} - \mathbf{u}^{0,h}\| \leq \underbrace{\|\mathbf{u} - \mathbf{u}^{00}\| + \|\mathbf{u}^{00} - \mathbf{u}^{0}\|}_{\text{modelling error}} + \underbrace{\|\mathbf{u}^{0} - \mathbf{u}^{0,h}\|}_{\text{Numerical error}} . \tag{3}$$

where $\mathbf{u}^{00}, \mathbf{u}^{0}$ are the solution of the second order and the first order homogenisation respectively, and h is the size of the coarse mesh. Modelling error from higher order homogenisations is neglected, and according to [1] and [35] the difference between solutions from second order homogenisation and first order homogenisation plays the main role in the modelling error in the presence of discontinuities:

$$\|\mathbf{u} - \mathbf{u}^{00}\| \ll \|\mathbf{u}^{00} - \mathbf{u}^{0}\| \tag{4}$$

Therefore, we devised a modelling error indicator based on the difference between the strain energy from second order homogenisation and the strain energy from first order homogenisation as in [1] to control the modelling error in our problem.

Two critical values are considered for the discretisation and the homogenisation errors. After each load step, whenever the discretisation error reaches its critical value, the corresponding coarse elements are refined. Then an evaluation of the homogenisation error is carried out over all coarse elements. Wherever the homogenisation error reaches its critical value, the scale adaptation is triggered, and the corresponding coarse elements are replaced by the underlying inhomogeneous problem. The discretisation error is first estimated and controlled by the refinement of the coarse scale mesh. Then, once the discretisation error has reached a predefined threshold, the modelling error is estimated and controlled by the scale adaptation procedure. We will adapt this scale-selection criterion to the context of multiscale nonlinear fracture mechanics problem in order to automatically track the vicinity of cracks that need to be described explicitly at the microscale for the macroscale response to be correctly predicted.

2. Microscale damage model for polycrystalline materials.

The two-dimensional grains, Ω^f, are modelled as linear elastic materials, separated by cohesive interfaces, Γ^f. Only inter-granular fracture is considered in this work. The Voigt's form of the constitutive relationship for the grains at the current configuration t is given by Hooke's law:

$$\forall \mathbf{x}^f \in \Omega^f \setminus \Gamma^f \quad \boldsymbol{\sigma}^f_{|_{\mathbf{x}^f,t}} = \mathbf{C}^f_{|_{\mathbf{x}^f}} \boldsymbol{\varepsilon}^f(\mathbf{u}^f_{|_{\mathbf{x}^f,t}}), \tag{5}$$

where the Cauchy stress and the strain at the microscale are denoted by $\boldsymbol{\sigma}^f$ and $\boldsymbol{\varepsilon}^f$ respectively, and $\mathbf{C}^f$ is a matrix that contains the elastic stiffness moduli of the grains. The superscript f indicates that the variables are defined at the microscale ("fine" scale). Note that the tensor form of the stress and strain will be represented by the same notation as used for their vector (Voigt's) form since they can be distinguished in context. The constitutive relationship for the interface between grains is based on a cohesive zone model and is given by:

$$\mathbf{T}^f(\mathbf{x}) = \mathbf{K}[\![\mathbf{u}^f(\mathbf{x})]\!], \quad \text{on } \Gamma^f, \tag{6}$$

where the traction and displacement jumps on the interface of the grains, Γ^f, are denoted by $\mathbf{T}^f$ and $[\![\mathbf{u}^f]\!]$ respectively. $\mathbf{K}$ is the damageable stiffness matrix given by a thermodynamically consistent function of the history of the displacement jump $[\![\mathbf{u}^f]\!]$ on the grain boundaries [46, 47]:

$$\mathbf{K} = \begin{bmatrix} k_n^+ (1-d)\, \mathcal{H}([\![u_n^f]\!]) + k_n^- \mathcal{H}(-[\![u_n^f]\!]) & 0 \\ 0 & k_t(1-d) \end{bmatrix}. \tag{7}$$

where k_t and k_n are original interface stiffness with dimension of force over length cubed for three dimension problems, and force over length squared for two-dimensional problems, and d is the damage parameter. The subscript t refers to the tangential direction of the interface while n refers to the normal to the interface. $[\![u_n]\!]$ and $[\![u_t]\!]$ are the normal and tangential component of the displacement jump $[\![\mathbf{u}]\!]$. In order to avoid the interpenetration of grains, the original interface stiffness for the closing mode is chosen to be much larger than the original interface stiffness for the opening mode, $k_n^-/k_n^+ > 1$. It is noted that a very large value of k_n^- causes ill-conditioning of the stiffness matrix in finite element procedure. In this study, we choose $k_n^-/k_n^+ = 100$. The Heaviside function $\mathcal{H}$ does not allow the damage parameter to influence the stiffness of the cohesive interface in compression mode. The damage parameter d is related to time history of the displacement jump $[\![\mathbf{u}^f]\!]$ in order to represent the irreversible fracture process. A power-law damage evolution is chosen:

$$d(\kappa) = \begin{cases} 0 & \kappa < \kappa_{\text{ini}} \\ 1 - \left(\frac{\kappa_{\text{ful}}-\kappa}{\kappa_{\text{ful}}-\kappa_{\text{ini}}}\right)^p & \kappa_{\text{ini}} < \kappa < \kappa_{\text{ful}} \\ 1 & \kappa > \kappa_{\text{ful}} \end{cases} \tag{8}$$

where p is a material variable. κ_{ini} and κ_{ful} are the thresholds of the internal variable κ that are associated with the initiation and the fully damaged conditions of the interface crack respectively. For time t, κ is given by:

$$\kappa(t) = \max\left(\kappa(\tau)_{\tau<t}; u_{\text{eff}}\right), \quad u_{\text{eff}} = \left\| \begin{matrix} [\![u_n]\!]\mathcal{H}([\![u_n]\!]) \\ a_t[\![u_t]\!] \end{matrix} \right\|, \tag{9}$$

The coefficient $a_t > 0$ controls the effect of shear jump on the damage parameter, and in this study $a_t = 1$. The function 'max' does not allow κ to decrease, and the Heaviside function $\mathcal{H}([\![u_n]\!])$ prevents the negative jump in normal direction $[\![u_n]\!] < 0$ (associated with compression mode) from having an influence on the damage variable.

We assume that the critical fracture energy of modes I and II and the maximum tensile and shear strengths are equal ($G_{Ic} = G_{IIc}$ and $\sigma_{\max} = \tau_{\max}$). The internal variable threshold κ_{ini} is assumed to be zero. The parameters introduced in the damage evolution law, Eq. (8), can be evaluated by the following equations [48]:

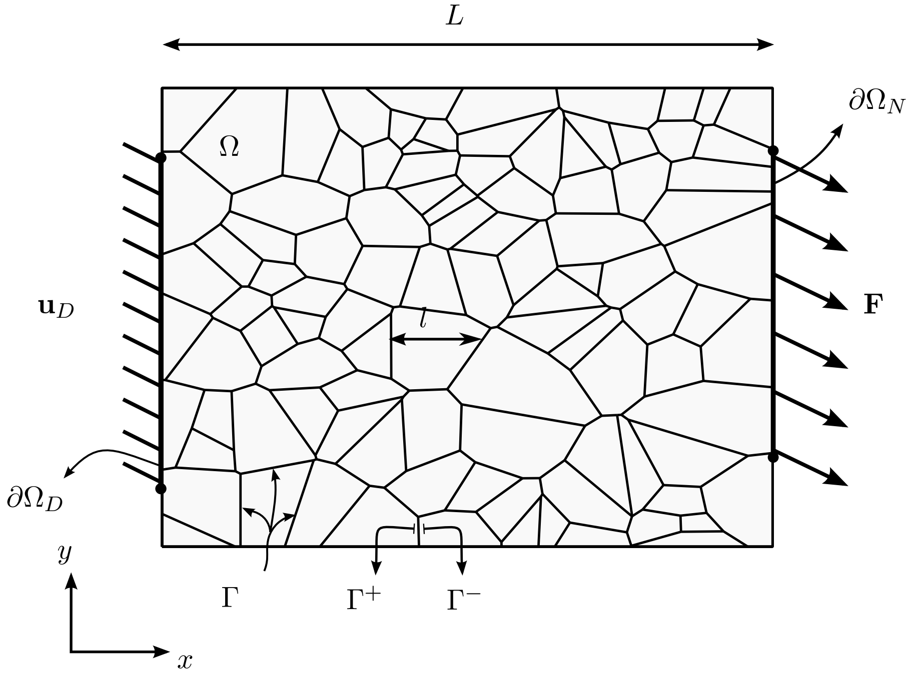

Figure 1. A schematic of the microscale problem

$$\kappa_{\text{full}} = [\![u]\!]_{\text{full}} = \alpha \frac{G_{Ic}}{\sigma_{\max}}, \quad \alpha = (n+2)\left(\frac{n}{n+1}\right)^{n} \tag{10}$$

$$k_n^+ = k_t = \beta \frac{\sigma_{\max}^2}{G_{Ic}}, \quad \beta = \frac{(n+1)}{(n+2)}\left(\frac{n+1}{n}\right)^{2n} \tag{11}$$

3. Hybrid multiscale framework

The fracture simulation is performed under the assumptions of quasi-static, isothermal evolution over time and small perturbations. The macroscopic problem is discretised by a coarse mesh which the finite elements cannot capture the heterogeneity of the microstructure. The macroscopic constitutive model is obtained by homogenisation of nonlinear microstructure. Cracks cannot propagate at the coarse scale, so the initiation and propagation of cracks are represented at the fine scale.

3.1. *FE^2 method*

We assume that the macroscopic constitutive equation cannot be efficiently derived in closed form at the macroscopic scale. Instead, it will be obtained implicitly through numerical material testing, which is the basic idea of the FE^2 method [2, 9, 49]. More precisely, incremental macroscopic stress-strain laws are obtained "on-the-fly" during the macroscopic solution process by solving the boundary value problem associated with the RVE at each (quadrature) point of the macroscopic FEM model. Micromechanics links micro and macro scales based on "average theorems" for strain, stress and energy. The average strain (respectively stress and energy) theorem assumes that the macroscopic strain (respectively stress and energy) at a particular macroscale point is equal to the average of the strain (stress or energy) of the corresponding RVE. For a microstructure with cohesive cracks, the average theorems are given by

$$\begin{aligned}
\boldsymbol{\varepsilon}^c &= \frac{1}{2|\mathcal{V}_\diamondsuit(\mathbf{x})|}\int_{\partial\mathcal{V}} \mathbf{u}^f \otimes \mathbf{n} + (\mathbf{u}^f \otimes \mathbf{n})^T \,\mathrm{d}\Gamma,\\
\boldsymbol{\sigma}^c &= \frac{1}{|\mathcal{V}_\diamondsuit(\mathbf{x})|}\int_{\partial\mathcal{V}} \mathbf{t}^f \otimes \mathbf{x}^f \,\mathrm{d}\Gamma,\\
\boldsymbol{\sigma}^c : \dot{\boldsymbol{\varepsilon}}^c &= \langle \boldsymbol{\sigma}^f : \dot{\boldsymbol{\varepsilon}}^f + \mathbf{t}^f \cdot [\![\dot{\mathbf{u}}]\!] \rangle = \frac{1}{|\mathcal{V}_\diamondsuit(\mathbf{x})|}\int_{\partial\mathcal{V}} \mathbf{t}^f \cdot \dot{\mathbf{u}}^f \,\mathrm{d}\Gamma,
\end{aligned} \tag{12}$$

where $|\mathcal{V}_\diamondsuit(\mathbf{x})|$ is the volume of RVE, $\mathcal{V}_\diamondsuit$, at the macroscopic point $\mathbf{x}$, and $\partial\mathcal{V}$ is the boundary of RVE. The unit outer vector normal to the RVE boundaries $\partial\mathcal{V}$ is denoted by $\mathbf{n}$, and the boundary tractions are denoted by $\mathbf{t}^f$. The last equation is consistent with Hill's energy consistency condition.

The macroscopic stress and tangent stiffness at the macroscopic quadrature points can be obtained by the micro-macro links provided by Eqs. 12. For more details see [48, 49].

3.2. *Domain decomposition method*

Bridging the scales by homogenisation is valid if scales are separable. When strain localisation happens, the homogenisation results become overly sensitive to the variation of both macroscopic mesh size and RVE size. In other words, an RVE cannot be found for softening regime which means that scales are not separable. In the critical regions where the scale separation assumption is not fulfilled, the FE^2 method is bypassed and a concurrent multiscale method based on domain decomposition is adopted. In the concurrent multiscale method the scale separation assumption does not need to be fulfilled, since the microscopic model is solved directly (see Fig. 2).

We have been investigating, in other settings, weak coupling techniques based on Nitsche's method (e.g. for NURBS patches, see [50–52]). Our experience of such coupling techniques is that they cause an increase in the conditioning number of the global system, which dramatically increases the required number of iterations to convergence when employing iterative solvers. Since direct solvers are not practical for the problem sizes we are discussing here, we decided to use strong coupling approaches instead.

We assume the existence of an equilibrated micro pair $(\mathbf{u}^f, \boldsymbol{\sigma}^f)$ defined over the fully resolved region Ω^f in equilibrium with the macro pair $(\mathbf{u}^c, \boldsymbol{\sigma}^c)$ at the coarse scale, defined over $\Omega^c = \Omega \backslash \Omega^f$. The weak form of the governing equations at arbitrary time t is given by:

$$\begin{cases}
\forall\,\delta\mathbf{u}^c \in \mathcal{U}^{c,0}, & \displaystyle\int_{\Omega^c} \boldsymbol{\sigma}^c : \boldsymbol{\varepsilon}(\delta\mathbf{u}^c)\,\mathrm{d}\Omega - \int_{\partial\Omega_N} \mathbf{F}\cdot\delta\mathbf{u}^c \mathrm{d}\Gamma = 0,\\
\forall\,\delta\mathbf{u}^f \in \mathcal{U}^{f,0}, & \displaystyle\int_{\Omega^f\backslash\Gamma^f} \boldsymbol{\sigma}^f : \boldsymbol{\varepsilon}(\delta\mathbf{u}^f)\,\mathrm{d}\Omega + \int_{\Gamma^f} \mathbf{T}^f \cdot [\![\delta\mathbf{u}^f]\!]\,\mathrm{d}\Gamma = 0,\\
\forall\,\mathbf{x} \in \Gamma^{fc}, & \mathbf{u}^c - \mathbf{u}^f = \mathbf{0}, \quad \text{and} \quad \boldsymbol{\sigma}^c\cdot\mathbf{n}^c = -\boldsymbol{\sigma}^f\cdot\mathbf{n}^f,
\end{cases} \tag{13}$$

where Ω^f and Ω^c are the fully resolved region and the coarse scale region respectively, with Γ^{fc} their intersection. The cohesive interfaces are denoted by Γ^f. The strong coupling of the fully resolved region Ω^f with the coarse domain Ω^c is en-

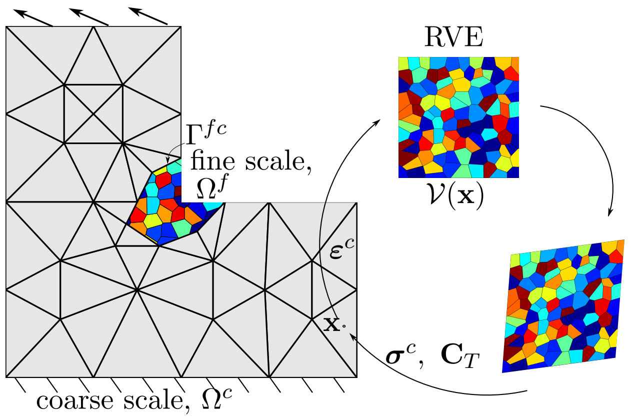

Figure 2. A hybrid multiscale method includes non-overlapping domain decomposition method and FE^2.

forced by the third equation in Eq. 13, where $\mathbf{n}^c$ and $\mathbf{n}^f$ are the normal outward vector of the coarse mesh and the fine mesh at the interface Γ^{fc}, respectively. These balance equations are complemented by the macroscopic (homogenised and defined through the solution of the RVE) and microscopic constitutive equations, and the Dirichlet boundary conditions, which are assumed to be enforced only on the boundary of the homogenised domain.

An implicit hybrid-scale time integration is carried out by using a local arc-length strategy for the multiscale domain decomposition problem that can robustly follow the load-displacement curve by imposing a constraint over the maximum increment of the displacement jump of all cohesive cracks within the fully resolved regions.

4. Adaptive scale selection

4.1. *Discrete representation of macroscale strain gradients: mesh adaptivity*

The coarse scale problem is solved by using standard linear triangular finite elements. In order to control the coarse mesh discretisation error, the Zienkiewicz-Zhu (ZZ) error estimate is employed [53] in association with local mesh subdivision. The classical SPR technique is used. Our experience of SPR-C and SPR-CX [54–57] compared to other non-equilibrated recovery techniques in the presence of discontinuities and singularities [58–60] shows that the benefits of enforcing consistency, local equilibrium, and boundary conditions is expensive and relatively complex to implement given the observed benefits. We decided to keep the recovery procedure simple and focused our efforts on the modelling error evaluation because whilst advanced techniques such as SPR-C and SPR-CX do decrease the error level and improve the effectivity of the error indicator and the convergence of the approximate error to the exact error, it is always possible, even without satisfying equilibrium, consistency and boundary conditions constraints, to obtain the same error level (with more refined meshes)[55].

After convergence of the nonlinear hybrid multiscale solver, and at any time step, those elements with high error in the energy norm are refined by splitting into four smaller elements. The adjacent elements are also split in order to make the mesh compatible.

In the adaptive multiscale method, after each mesh refinement, some modifications are required before starting a new time step:

- The RVEs corresponding to the parent elements are copied to the new, finer elements.

- The homogenisation error is computed and the scale adaptation condition is checked. If the error of homogenisation is larger than the critical value, the corresponding coarse elements are replaced by an explicit representation of the microstructure (see next section).
- After mesh refinement or microstructure adaptation, the residual force will be out of balance due to disturbances in the internal force. We relax the out-of-balance force by running the nonlinear iterative solver before starting the next load step.

4.2. *Modelling error control: scale adaptivity*

In the previous section, we have described how the representation of macroscale strain gradients is controlled by refinement of the finite element mesh. The error due to the partial fulfilment of the scale separation will now be estimated by making use of these coarse-scale gradients. Indeed, scale separation is lost in regions where these gradients are large compared to the typical size of the microstructural constituents. This observation will be the basis for the developments proposed in this section.

In order to determine the loss of accuracy for first order homogenisation [1] and [35] developed two error indicators. The main concept of their error indicators is based on the difference between the strain energy from second order homogenisation and the strain energy from first order homogenisation.

More precisely, [1] assumes that the difference between the (unknown) fine-scale solution and the computed macroscopic surrogate is well-represented by the difference between macroscopic surrogate and the solution delivered by a second-order macroscopic homogenised problem. Secondly, the authors claim that a good indicator for this local homogenisation error is obtained by measuring the local difference of energy delivered by first and second order homogenisation schemes. After running a series of test on the RVE of an hyper-elastic microstructure with various degrees of material heterogeneity, deformation and deformation gradient, they finally show that this local difference is a monotonically increasing function of $L_{\mathcal{V}}||\nabla\nabla\mathbf{u}^c||$ which they referred to as the strain-gradient sensitivity. Here, $L_{\mathcal{V}}$ is the size of the RVE, and $||\nabla\nabla\mathbf{u}^c||$ is the Euclidean norm of the second gradient of the displacement field that can be written in Einstein's notation as $||\nabla\nabla\mathbf{u}^c|| = \sqrt{u^c_{i,jk}u^c_{i,jk}}$.

Following [35] and [1], the strain-gradient sensitivity is chosen as local error indicator for the error of homogenisation e_h. The criterion for scale adaptation reads:

$$L_{\mathcal{V}}||\nabla\nabla\mathbf{u}^c||_e > e_h^{\text{crit}}, \tag{14}$$

Whenever this criterion is satisfied, the corresponding macroscale element e is replaced by the underlying microstructure,

The scale adaptation criterion requires the evaluation of the local deformation gradients. We do not wish to solve the higher-order homogenisation scheme. Instead, and consistently with [1, 35], the deformation gradients are recovered from the first-order homogenisation scheme, using local post-processing. In this paper, we recall that we use linear macro elements, and that we employ a recovery-based technique [53] for error estimation. Therefore, it is natural to use the smoothing of the ZZ error estimate to define our approximation of the deformation gradients. The details of this implementation are given in Appendix A.

The arbitrary shapes of the grains do not coincide with the coarse element edges. The critical coarse elements which are flagged by the homogenisation error criterion, create a window to the underlying grains. To match the two different geome-

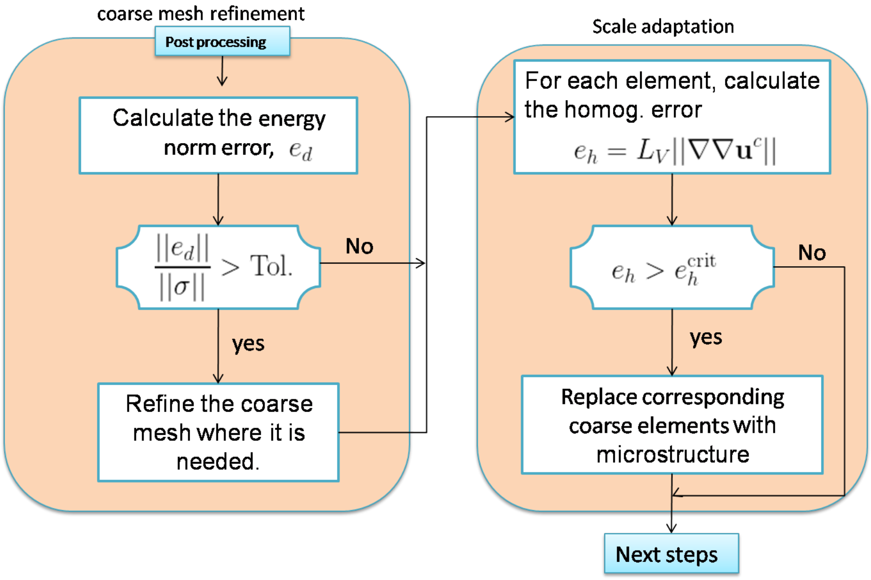

Figure 3. Flowchart of the proposed adaptive multiscale method, carried out at the end of each load increment.

tries, the underlying grains are cut and tailored according to the window of the critical coarse elements. The fully resolved regions were adaptively expanded to the new critical zones where the coarse elements have a modelling error $e_h > e_h^{\text{crit}}$ or when their corresponding RVEs have already lost the stability.

Figure 4 demonstrates the procedure of the development of a fully resolved region schematically. The procedure is slightly different for the initiation of a fully resolved region than the extension of it. A five-step zoom-in procedure can be employed for the extension of an existing fully resolved region (the right column in Fig. 4), while the third step can be skipped for the initiation of the fully resolved region (the left column in Fig. 4).

A zoom-in procedure is started when a critical zone appears at the coarse scale due to excessive homogenisation error. The underlying microstructre of the critical zone is determined by opening a window to the actual microstructure. It is assumed that the actual geometry of the microstructure is known *a priori*. In the third step, if the new critical zone is an extension to an existing fully resolved region, those grains that are common between the existing fully resolved region and its extension are attached to the extension part, and all related data are dismissed. In the fourth step, the extension part is meshed in such a way that the mesh is compatible with the adjacent coarse mesh and fully matches with the adjacent fully resolved regions. The fourth step also consists of an equalisation process that solves the new fully resolved region boundary value problem based on the history of displacement field that has been experienced by the critical zone. At the end of equalisation process, the displacement field of the new fully resolved region is compatible with the surrounding meshes, and the level of energy saved in the high resolution region is approximately equal to the amount of strain energy in the coarse elements before adaptation [48]. In the next step, the Linear Multiple Point Constraint (LMPC) technique is used to couple the the new fully resolved region to the rest of the domain. Finally, before continuing the simulation, a relaxation procedure is performed to minimise the out-of-balance residual force.

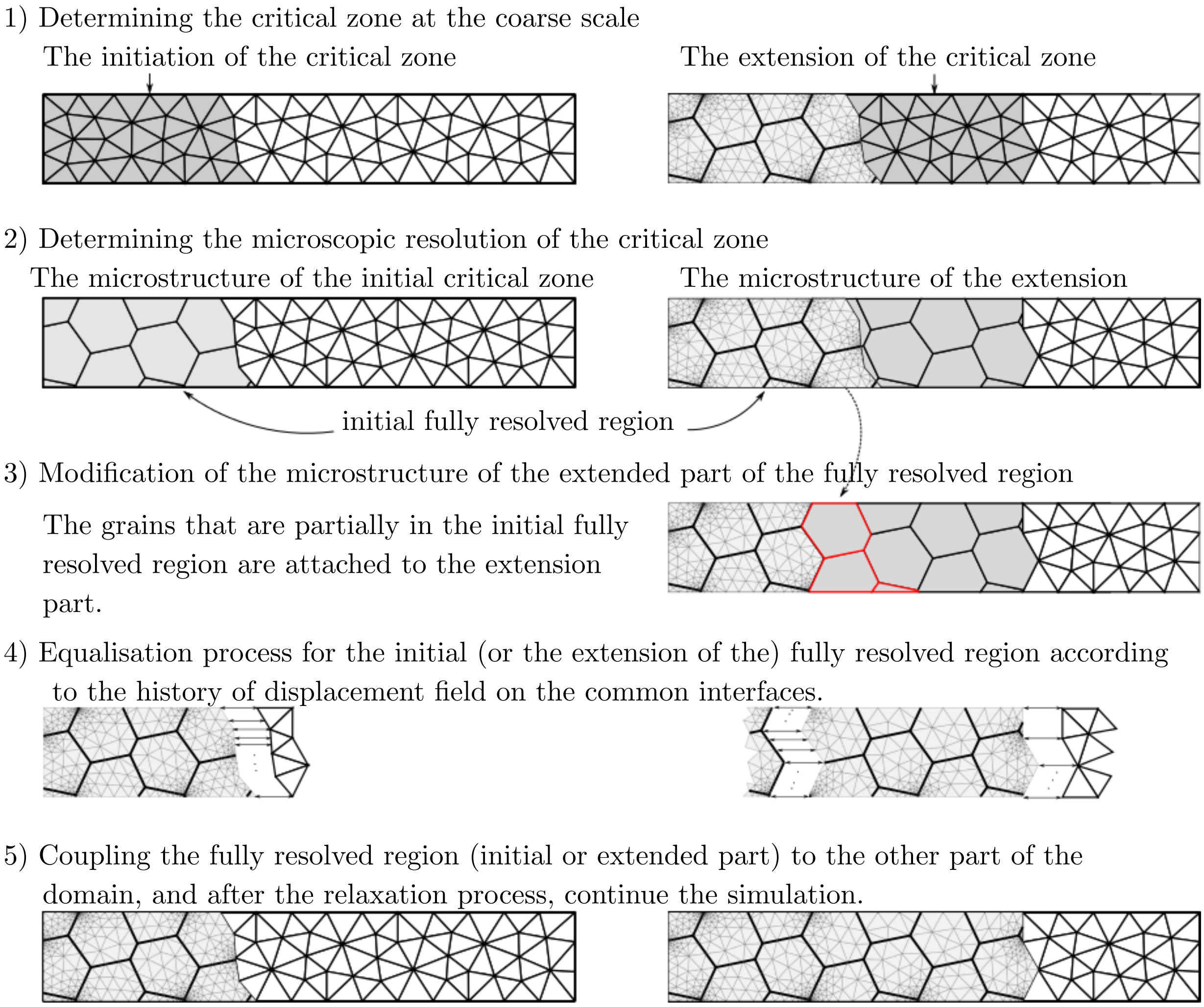

Figure 4. The procedure of the development of the fully resolved region

Table 1. Microscale material parameters.

grain			cohesive interface			
E	ν	l_g	$\sigma_{\max} = \tau_{\max}$	$G_{Ic} = G_{IIc}$	κ_{ini}	n
384.6GPa	0.237	25μm	1 GPa	35 Jm^{-2}	0	0.5

5. Results and discussion

To illustrate the proposed methodology, a single-notched beam under uni-axial load is considered, as shown in Fig. 5. The results from the proposed multiscale framework are compared to those from a direct numerical solution (DNS). The beam is made of a polycrystalline material, for which the constitutive equations were introduced in Section 2, and the mechanical properties of the grains are given in Table 1. The critical value of strain-sensitivity $e_h^{crit} = 0.01$ for this example.

In order to decrease computational costs a priori, the FE^2 method is only implemented in the middle part of the beam (grey region in Fig. 5), and a constant linear elastic homogenised model with Young's modulus $E = 386.4$ GPa and Poisson's Ratio $\nu = 0.237$ is employed for the rest of the domain. For consistency reasons, only the middle region is resolved at the microscale in the DNS.

Distribution of the von Mises stress over the notched beam are shown in Fig. 6

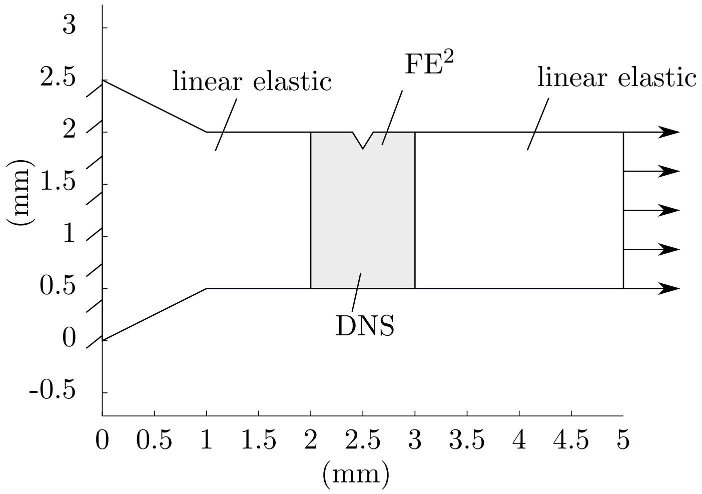

Figure 5. Single-notched beam under uni-axial tensile load. The grey region is solved using the adaptive hybrid multiscale approach.

for the DNS and the adaptive multiscale solution. We obtain very similar stress distributions in these two cases. The maximum stress appears at the crack tip as expected. Notice that in the cohesive interface models, the crack tip stress is not infinite, and it is related to the maximum failure stress of the cohesive interface (see Eq. (10)).

As developed in Section 4.1, the ZZ error estimator is employed for the control of the macroscale discretisation space, and the strain-gradient sensitivity is used as a measurement for the homogenisation error. The maximum permissible discretisation error is set to $\bar{\eta} = 5\%$. Whenever the strain-gradient sensitivity of a coarse element $L_{\mathcal{V}}||\nabla\nabla\mathbf{u}^c||_e$ becomes larger than the critical value of the homogenisation error, the microstructure corresponding to this element is fully resolved. As a first attempt to reproduce the DNS computation, the critical value of the homogenisation error indicator is set to $e_h^{\text{crit}} = 0.01$.

The distribution of the strain-gradient sensitivity of the coarse mesh is illustrated in Fig. 7. The strain-gradient sensitivity remains small during the first time steps of the simulation. With increasing load, the homogenisation error indicator increases at the notch. Consequently the coarse elements with highest error levels are replaced by the underlying microstructure (Time steps of index greater than >5 in the figure). Subsequently, cracks initiate and propagate at the grain boundaries, within the explicitly resolved microscopic region. It is observed that most of the coarse elements in the vicinity of the macroscale crack tip have high strain-gradient sensitivities.

As shown in this figure, the adaptive procedure correctly follows the crack path, without any prior knowledge.

In Fig. 8, the coarse mesh in the vicinity of the fully resolved region is shown. Our choice of scale selection criterion and associated threshold value allows some of the coarse elements to be smaller than the size of a grain.

The energy dissipation due to crack propagation has been investigated as a quantitative indicator of the validity of the proposed approach. For the notched beam, the variation of the external work W_{ext}, total strain energy W_{int}, and the dissipated energy D versus time are shown in Fig. 9. The beam reaches its maximum strain energy at time step 8. During subsequent time steps, the external load is decreased in order to accommodate the snap-back behaviour of the load-displacement curve. The level of external work and the strain energy of the structure drop drastically (Time step 15). In this stage, the grains around the notch get separated, and a

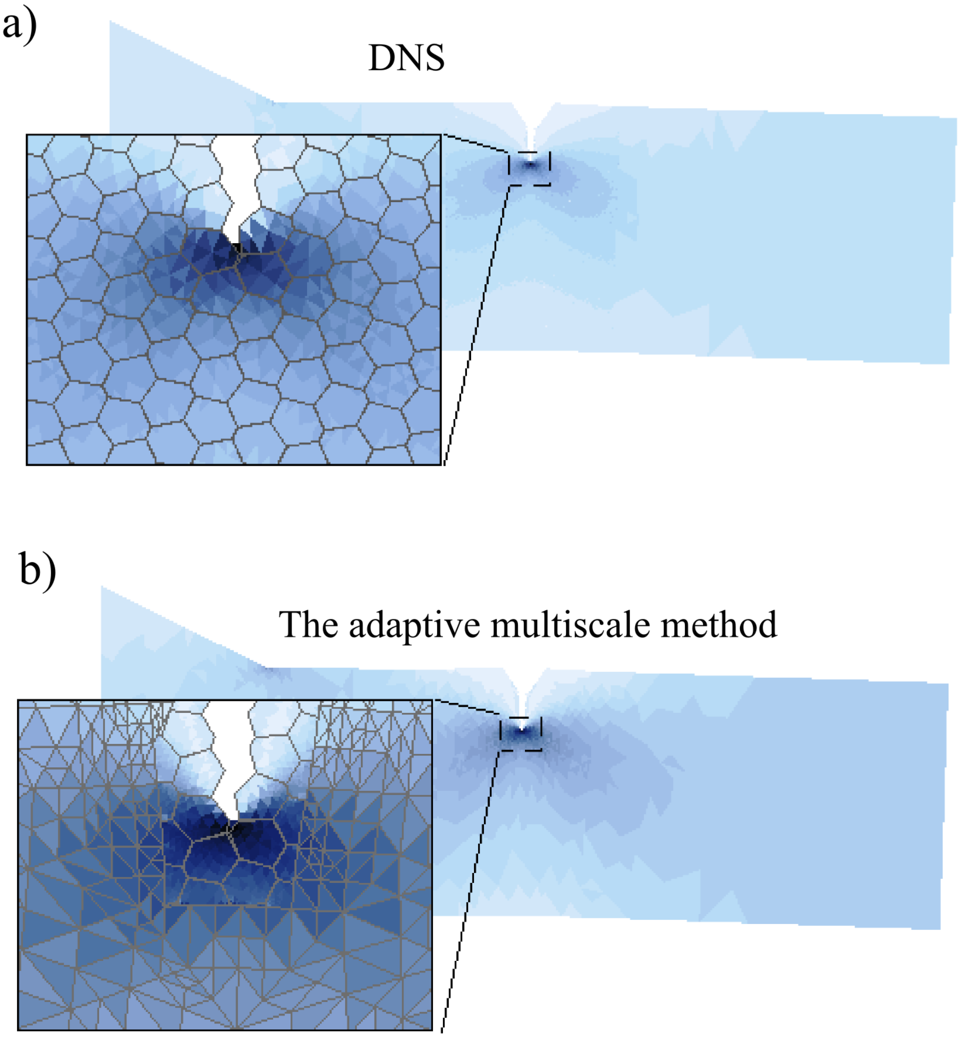

Figure 6. Von Mises stress distribution in the notched bar a) DNS and b) Adaptive multiscale solution. Deformation is magnified by 100.

macro-crack is nucleated. Although the strain energy and the external work display oscillations, the dissipated energy of the beam increases in a strictly monotonic manner. This is because the employed arc-length techniques enforces that the cohesive cracks dissipate a given amount of energy during each time step. The external work W_{ext}, the total strain energy W_{int} and the dissipated energy D of the beam

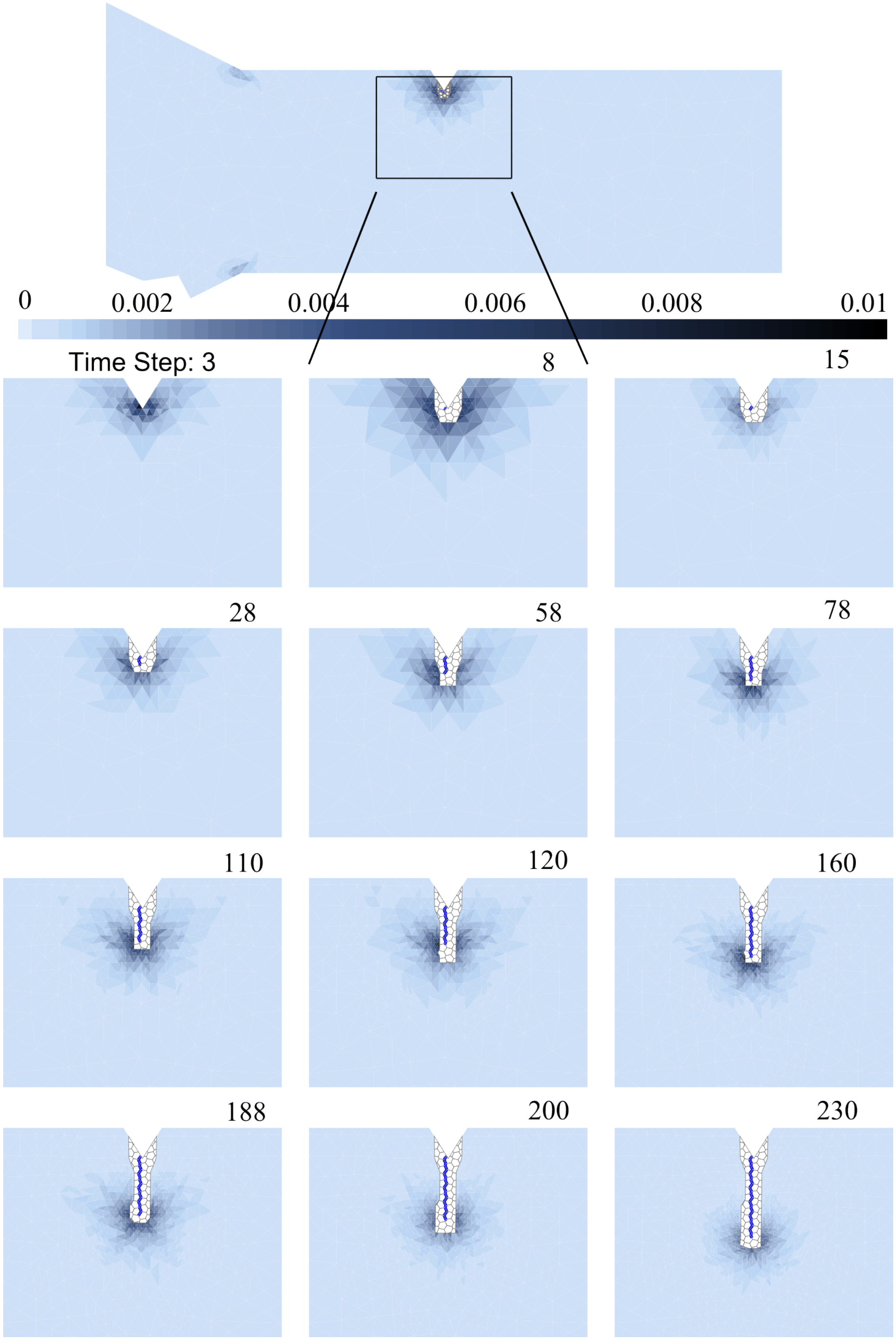

Figure 7. The distribution of strain-gradient sensitivity $L_{\mathcal{V}}||\nabla\nabla\mathbf{u}^c||_e$, and the adaptive development of the fully resolved region.

at time t were calculated as follows:

$$W_{\text{ext}}(t) = \sum_{i=1}^{n_t}\left(\int_{\partial\Omega_N}\mathbf{F}|_{\tau_i}\cdot\Delta\mathbf{u}^{\mathbf{c}}|_{\tau_i}\ \mathrm{d}\Gamma\right), \tag{15}$$

$$W_{\text{int}}(t) = \frac{1}{2}\int_{\partial\Omega_N}\mathbf{F}|_{\tau_{n_t}}\cdot\mathbf{u}^{\mathbf{c}}|_{\tau_{n_t}}\ \mathrm{d}\Gamma, \tag{16}$$

$$D(t) = W_{\text{ext}}(t) - W_{\text{int}}(t), \tag{17}$$

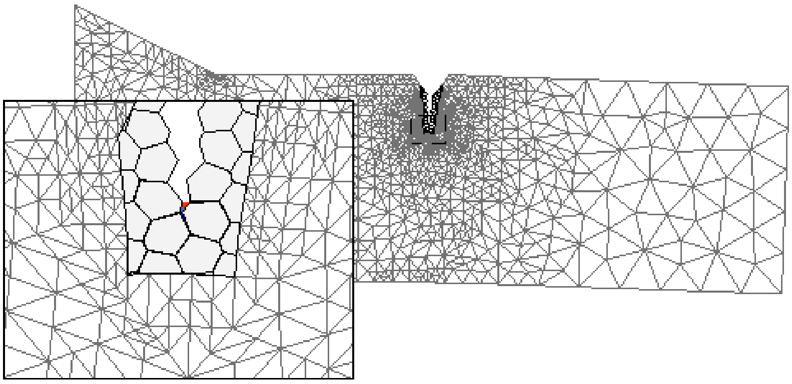

Figure 8. Coarse mesh in the adaptive multiscale at Time step 200. Deformation is magnified by 100.

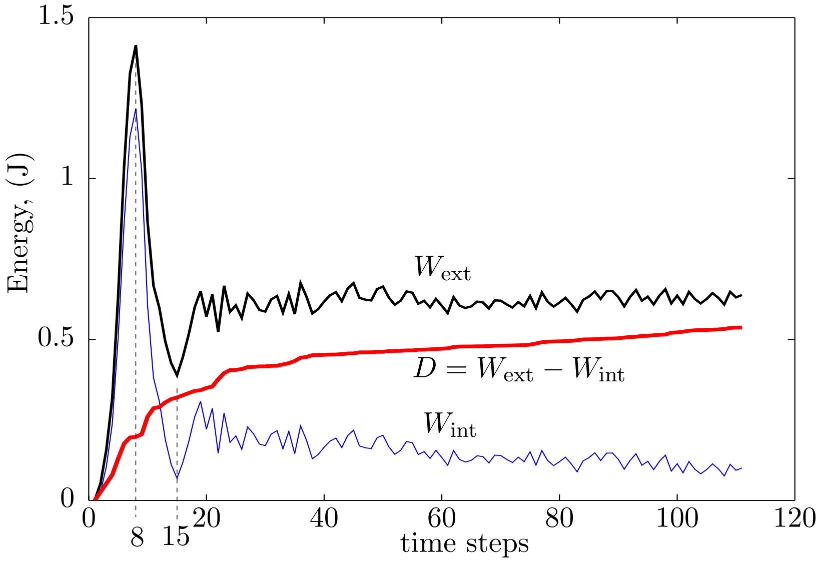

Figure 9. Variation of the external work W_{ext}, the stored elastic energy W_{int}, and the dissipated energy D in a notched beam under a uni-axial load.

where $\Delta\mathbf{u^c}|_{\tau_i}$ is the variation of the macroscopic displacement over the i^{th} time step τ_i, and $\mathbf{F}$ is the external traction load on the Neumann boundary $\partial\Omega_N$. The total number of time steps are denoted by n_t and the current time is denoted by $t = \tau_{n_t}$.

In Fig. 10, the deformation of the fully resolved region at two time steps is shown: 1) time step 8 when the domain is experiencing its maximum level of strain energy, and 2) time step 15 when the crack is initiated and the strain energy of the domain drops. Due to the micro-crack nucleation at time step 15, the beam is unloaded and therefore the V-shape notch is less deformed in comparison to the deformation that are observed at time step 8. As shown in the Fig. 9, the elastic energy at time step 15 is lesser than the total energy computed at time step 8.

The energy dissipation in the beam versus the displacement at the tip of the

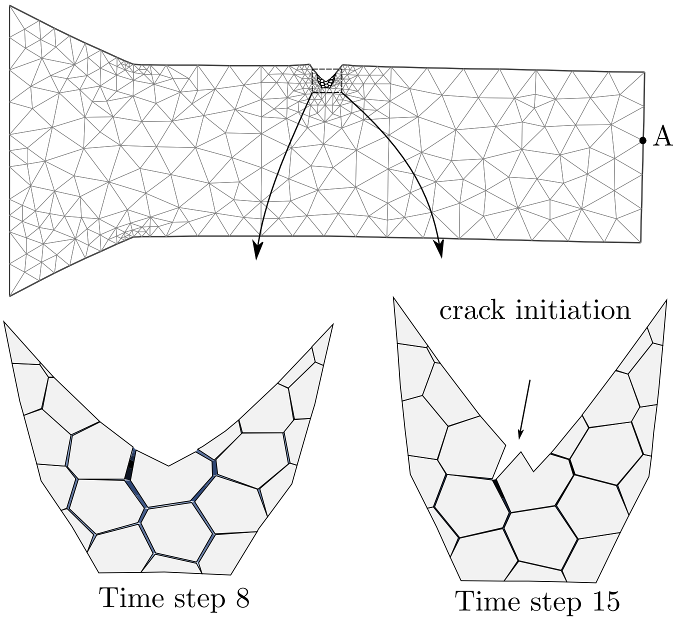

Figure 10. Capturing the crack initiation at the grain scale using adaptive multiscale method. Deformation is magnified by 100.

beam is shown in Fig. 11, where the result from the adaptive multiscale method is compared to the results obtain using DNS. It is observed that the total dissipated energy D obtained from the adaptive multiscale method is lesser than the dissipated energy from the DNS for the same displacement.

In Fig. 12, the dissipated energy is plotted as a function of a measure of the cracked area for both the adaptive multiscale method and the DNS computations. To calculate the cracked area , the cohesive cracks with damage parameter d larger than 0.423 are considered as fully opened. Most of the cohesive interfaces undergo some level of damage but can still carry the load except those interfaces with $d > 0.423$. This is because the traction-separation law transitions to the softening regime when $d > 1-\left(\frac{n}{n+1}\right)^n$. The energy dissipated before macro-crack initiation in the DNS is 10% more than that in the adaptive multiscale method. The rate of energy dissipation in the DNS is also higher than the rate of energy dissipation obtained from the adaptive multiscale method. This mismatch is attributed to (i) the Dirichlet conditions between coarse and small domain, which stiffen the structure and prevent damage diffusion, and too loose a strain sensitivity threshold, and (ii) the small size of the RVE employed for homogenisation and the uniform Dirichlet BC.

6. Conclusion

We have proposed a method to automatically choose the scale of material representation in nonlinear fracture mechanics. Starting from an homogenised representation of the microstructure, regions where loss of scale separability produces inadmissible level of modelling errors are adaptively solved at the microscale.

In order to locate these regions, the homogenisation error indicator, proposed initially in [1] has been adapted to the context of fracture mechanics. This criterion is based on a measure of the macroscale strain gradients. We further proposed to obtain these macroscale strain gradients in a reliable manner by using error-driven

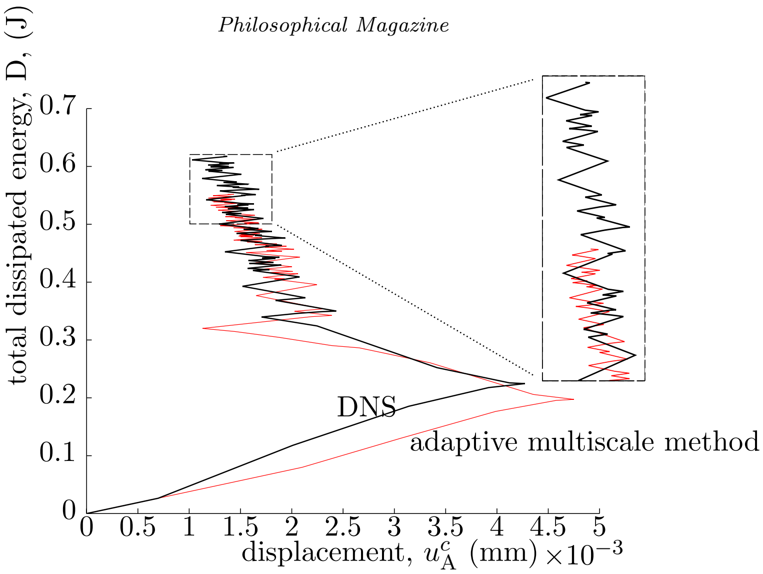

Figure 11. The variation of dissipated energy D versus displacement at the Neumann boundary of notched beam (Point A in Fig. 10).

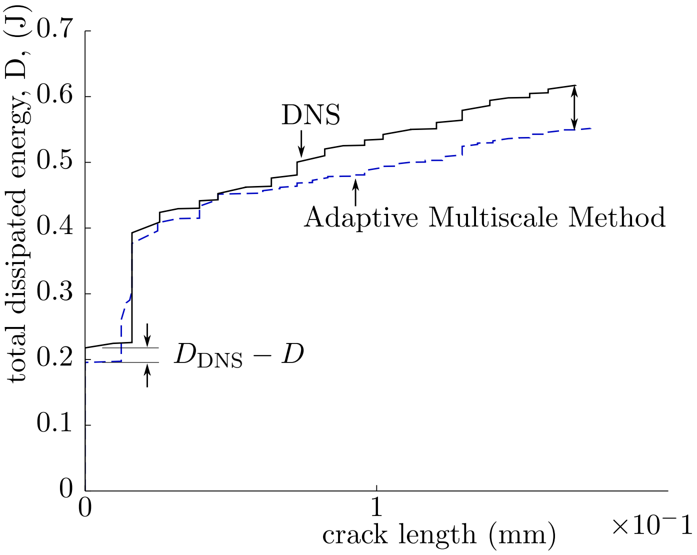

Figure 12. The variation of dissipated energy D versus crack area.

mesh adaptation and efficient recovery procedures.

We demonstrated the validity of this approach by simulating the propagation of a crack in a two dimensional notched bar. The results obtained using the proposed method were compared to those obtained using direct numerical solution. We have shown that crack initiations and propagations could be tracked automatically and that the approach concentrates the numerical effort due to explicit microscale representations to the cracked region. We showed that due to our choices for the parameters of the hybrid multiscale approach, in particular the size of kinematically-driven RVE, the kinematic strong coupling between homogenised and microscale regions and the threshold value for the modelling error indicator, the method tends to underestimate the amount of dissipation occurring in the structure.

Further studies are required to test the robustness and stability of the method, and the efficiency of the strain-sensitivity criterion as a measure of local modelling error in the context of fracture mechanics.

Acknowledgement

The authors would like to acknowledge partial financial support of the Framework Programme 7 Initial Training Network Funding under grant number 289361“Integrating Numerical Simulation and Geometric Design Technology” and of EPSRC under grant “Towards rationalised computational expense for simulating fracture over multiple scales (RationalMSFrac)”. The authors would also like to thank the financial support of the School of Engineering at Cardiff University for Dr Ahmad Akbari Rahimabadi PhD. Ahmad Akbari would also like to acknowledge the financial support of the Framework Programme 7 under IRSES exchange programme for his visit to the University of Witwatersrand in Johannesburg, South Africa.

Appendix A

In this appendix, a smoothing process is designed to obtain the second gradient of displacement for triangular linear elements. The displacement gradient tensor for each element $\nabla \mathbf{u}^c = \frac{\partial u_i}{\partial x_j}$ can be be obtained in vector form:

$$\forall e \in \Omega^c, \quad \nabla \mathbf{u}^c_e = \begin{Bmatrix} \frac{\partial u^c}{\partial x} \\ \frac{\partial v^c}{\partial y} \\ \frac{\partial u^c}{\partial y} \\ \frac{\partial v^c}{\partial x} \end{Bmatrix}_e = \begin{bmatrix} \frac{\partial N_1}{\partial x} & 0 & \frac{\partial N_2}{\partial x} & 0 & \frac{\partial N_3}{\partial x} & 0 \\ 0 & \frac{\partial N_1}{\partial y} & 0 & \frac{\partial N_2}{\partial y} & 0 & \frac{\partial N_3}{\partial y} \\ \frac{\partial N_1}{\partial y} & 0 & \frac{\partial N_2}{\partial y} & 0 & \frac{\partial N_3}{\partial y} & 0 \\ 0 & \frac{\partial N_1}{\partial x} & 0 & \frac{\partial N_2}{\partial x} & 0 & \frac{\partial N_3}{\partial x} \end{bmatrix}_e \begin{Bmatrix} U^c_1 \\ V^c_1 \\ U^c_2 \\ V^c_2 \\ U^c_3 \\ V^c_3 \end{Bmatrix}_e . \tag{18}$$

Since linear shape functions are employed, the displacement gradient over each element is constant. By making use of a simple averaging technique, the nodal value of the displacement gradient tensor are obtained:

$$\bar{\nabla}_I \mathbf{u}^c = \frac{1}{n_I} \sum_{e=1}^{n_I} \nabla \mathbf{u}^c. \tag{19}$$

where $\bar{\nabla}_I$ stands for the nodal value of gradient and n_I is the number of elements related to node I.

Then, an approximation of exact displacement gradient can be obtained by interpolating the nodal values of displacement gradient:

$$\forall \mathbf{x} \in \Omega^c_e, \quad \nabla^* \mathbf{u}^c(\mathbf{x}) = \sum_I N_I(\mathbf{x}) \bar{\nabla}_I \mathbf{u}^c, \tag{20}$$

where ∇^* indicates the recovery-based gradient, and N_I is the nodal shape function that is being used for displacement interpolation.

Finally, the second displacement gradient can be derived from the recovery-based first displacement gradient field:

$$\forall \mathbf{x} \in \Omega^c_e, \quad \nabla \nabla^* \mathbf{u}^c(\mathbf{x}) = \sum_I \mathbf{B}_I(\mathbf{x}) \bar{\nabla} \mathbf{u}^c_e, \tag{21}$$

where $\mathbf{B}_I$ is a matrix that contains the shape function gradients for node I:

$$\mathbf{B}_I = \begin{bmatrix} \frac{\partial N_I}{\partial x} & 0 & 0 & 0 \\ 0 & \frac{\partial N_I}{\partial y} & 0 & 0 \\ \frac{\partial N_I}{\partial y} & 0 & 0 & 0 \\ 0 & 0 & \frac{\partial N_I}{\partial x} & 0 \\ 0 & \frac{\partial N_I}{\partial x} & 0 & 0 \\ 0 & 0 & 0 & \frac{\partial N_I}{\partial y} \\ 0 & 0 & \frac{\partial N_I}{\partial y} & 0 \\ 0 & 0 & 0 & \frac{\partial N_I}{\partial x} \end{bmatrix}, \tag{22}$$

and consequently, the second gradient tensor is given in vector form:

$$\nabla\nabla^{*}\mathbf{u}^{c}(\mathbf{x}) = \left[\frac{\partial^2 u}{\partial x^2}, \frac{\partial^2 v}{\partial y^2}, \frac{\partial^2 u}{\partial x \partial y}, \frac{\partial^2 u}{\partial y \partial x}, \frac{\partial^2 v}{\partial x \partial y}, \frac{\partial^2 v}{\partial y \partial x}, \frac{\partial^2 u}{\partial y^2}, \frac{\partial^2 v}{\partial x^2}\right]^T \tag{23}$$

At the end, the norm of second displacement gradient for each element is approximated by the square root of the inner product of $\nabla\nabla^{*}\mathbf{u}^{c}(\mathbf{x})$

$$||\nabla\nabla\mathbf{u}^{c}|| = \sqrt{\nabla\nabla\mathbf{u}^{c} \vdots \nabla\nabla\mathbf{u}^{c}} \simeq \sqrt{(\nabla\nabla^{*}\mathbf{u}^{c})^{T}\nabla\nabla^{*}\mathbf{u}^{c}} \tag{24}$$

References

[1] I. Temizer and P. Wriggers, Computer Methods in Applied Mechanics and Engineering 200 (2011), pp. 2639–2661.

[2] F. Feyel and J.l. Chaboche, Computer Methods in Applied Mechanics and Engineering 183 (2000), pp. 309–330.

[3] J. Fish, K. Shek, M. Pandheeradi, and M.S. Shephard, Computer Methods in Applied Mechanics and Engineering 148 (1997), pp. 53–73.

[4] C. Miehe, M. Becker, and J. Schruder, Computer Methods in Applied Mechanics and Engineering 191 (2002), pp. 4971–5005.

[5] T.I. Zohdi and P. Wriggers, *An introduction to computational micromechanics*, Springer, 2008.

[6] E.W.C. Coenen, V.G. Kouznetsova, and M.G.D. Geers, International Journal for Numerical Methods in Engineering 83 (2010), pp. 1180–1205.

[7] P. Kerfriden, J.J. Ródenas, and S.P.A. Bordas, International Journal for Numerical Methods in Engineering 97 (2014), pp. 395–422.

[8] E. Sanchez-Palencia, *Homogenisation in mechanics: A survey of solved and open problems*, in *Conferenze di Fisica e di Mathematica*, Vol. 44, Università e Politecnico di Torino, Torino, 1986, pp. 1–46.

[9] P.M. Suquet, *Elements of homogenization for inelastic solid mechanics*, in *Homogenization Techniques for Composite Media*, Springer-Verlag, 1987, pp. 193–198.

[10] G. Allaire, SIAM J. MATH. ANAL. 23 (1992), pp. 1482–1518.

[11] S. Nemat-Nasser and M. Hori, *Micromechanics: Overall Properties of Heterogeneous Materials*, Vol. 1, 2nd ed., Amsterdam: Elsevier, 1999.

[12] G.W. Milton, *The Theory of Composites*, Cambridge Monographs on Applied and Computational Mathematics, Cambridge University Press, 2002.

[13] Y. Efendiev and T.Y. Hou, *Multiscale finite element methods: Theory and applications*, Vol. 2, Springer, 2009.

[14] G. Allaire, ESAIM: Proceedings 37 (2012), pp. 1–49.

[15] W. Chen and J. Fish, Journal of Applied Mechanics 68 (2001), pp. 153–161.

[16] S. Forest, F. Pradel, and K. Sab, International Journal of Solids and Structures 38 (2001), pp. 4585–4608.

[17] Y. Wang, R. Ballarini, and G.J. Rodin, Journal of Engineering Mechanics 134 (2008), pp. 100–109.

[18] P. Kerfriden, O. Allix, and P. Gosselet, Computational Mechanics 44 (2009), pp. 343–362.

[19] J.F. Unger and S. Eckardt, Archives of Computational Methods in Engineering 18 (2011), pp. 341–393.

[20] O. Lloberas-Valls, D.J. Rixen, A. Simone, and L.J. Sluys, Computer Methods in Applied Mechanics and Engineering 225-228 (2012), pp. 177–196.

[21] A. Ghosh and P. Chaudhuri, Computational Materials Science 69 (2013), pp. 204–215.

[22] H. Talebi, M. Silani, S.P.A. Bordas, P. Kerfriden, and T. Rabczuk, Computational Mechanics (2013), pp. 1–25.

[23] L.A.A. Beex, P. Kerfriden, T. Rabczuk, and S.P.A. Bordas, Computer Methods in Applied Mechanics and Engineering 279 (2014), pp. 348–378.

[24] M.J. Buehler and H. Gao, *Ultra large scale simulations of dynamic materials failure*, in *Handbook of Theoretical and Computational Nanotechnology*, Vol. X, chap. 14, American Scientific Publishers, 2005, pp. 1–41.

[25] P. Kerfriden, O. Goury, T. Rabczuk, and S.P.A. Bordas, Computer Methods in Applied Mechanics and Engineering 256 (2013), pp. 169–188.

[26] S. Loehnert and T. Belytschko, International Journal for Numerical Methods in Engineering 71 (2007), pp. 1466–1482.

[27] H. Ben Dhia, Comptes Rendus de l'Academie des Sciences Series IIB Mechanics Physics Astronomy 326 (1998), pp. 899–904.

[28] C. Bernardi, Y. Maday, and F. Rapetti, GAMM-Mitt 28 (2005), pp. 97–123.

[29] A. Mobasher Amini, D. Dureisseix, and P. Cartraud, International Journal For Numerical Methods In Engineering 79 (2009), pp. 417–443.

[30] S. Ghosh, K. Lee, and P. Raghavan, International Journal of Solids and Structures 38 (2001), pp. 2335–2385.

[31] T.I. Zohdi, J.T. Oden, and G.J. Rodin, Computer Methods in Applied Mechanics and Engineering 138 (1996), pp. 273–298.

[32] A. Romkes, J.T. Oden, and K. Vemaganti, Mechanics of Materials 38 (2006), pp. 859–872.

[33] S. Ghosh, J. Bai, and P. Raghavan, Mechanics of Materials 39 (2007), pp. 241–266.

[34] F. Larsson and K. Runesson, Computer Methods in Applied Mechanics and Engineering 200 (2011), pp. 2662–2674.

[35] F.J. Vernerey and M. Kabiri, Computer Methods in Applied Mechanics and Engineering 241-244 (2012), pp. 52–64.

[36] J.T. Oden and T.I. Zohdi, Computer Methods in Applied Mechanics and Engineering 148 (1997), pp. 367–391.

[37] J.T. Oden and K.S. Vemaganti, jornal of Computational Physics 47 (2000), pp. 22–47.

[38] A. Romkes and J.T. Oden, Computer Methods in Applied Mechanics and Engineering 193 (2004), pp. 539–559.

[39] P.T. Bauman, J.T. Oden, and S. Prudhomme, Computer Methods in Applied Mechanics and Engineering 198 (2009), pp. 799–818.

[40] H.B. Dhia, L. Chamoin, J.T. Oden, and S. Prudhomme, Computer Methods in Applied Mechanics and Engineering 200 (2011), pp. 2675–2696.

[41] S. Prudhomme, L. Chamoin, H.B. Dhia, and P.T. Bauman, Computer Methods in Applied Mechanics and Engineering 198 (2009), pp. 1887–1901.

[42] T.I. Zohdi and P. Wriggers, International Journal of Solids and Structures (1999).

[43] T.I. Zohdi, P. Wriggers, and C. Huet, Computer Methods in Applied Mechanics and Engineering 190 (2001), pp. 5639–5656.

[44] T.I. Zohdi and P. Wriggers, Archives of Computational Methods in Engineering 8 (2001), pp. 131–228.

[45] T.I. Zohdi, Journal of Elasticity 58 (2000), pp. 249–255.

[46] O. Allix, P. Kerfriden, and P. Gosselet, International Journal for Numerical Methods in Engineering 11 (2010), pp. 1518–1540.

[47] O. Allix and A. Corigliano, International Journal of Fracture 77 (1996), pp. 111–140.

[48] A. Akbari Rahimabadi, *Error controlled adaptive multiscale method for fracture in polycrystalline materials*, Phd thesis, Engineering, Cardiff University, 2014.

[49] V.G. Kouznetsova, W.A.M. Brekelmans, and F.P.T. Baaijens, Computational Mechanics 27 (2001), pp. 37–48.

[50] V.P. Nguyen, P. Kerfriden, M. Brino, S.P.A. Bordas, and E. Bonisoli, Computational Mechanics 53 (2014), pp. 1163–1182.

[51] V.P. Nguyen, P. Kerfriden, S. Claus, and S.P.A. Bordas, Tech. Rep., Cardiff University.

[52] V.P. Nguyen, S. Bordas, and T. Rabczuk, arXiv preprint arXiv:1205.2129 (2012).

[53] O.C. Zienkiewicz and J.Z. Zhu, International Journal for Numerical Methods in Engineering 24 (1987), pp. 337–357.

[54] J. Ródenas, O. González-Estrada, P. Díez, and F. Fuenmayor, Computer Methods in Applied Mechanics and Engineering 199 (2010), pp. 2607–2621.

[55] O.A. GonzálezEstrada, J.J. Ródenas, S.P.A. Bordas, M. Duflot, P. Kerfriden, and E. Giner, Engineering Computations 29 (2012), pp. 814–841.

[56] O.A. González-Estrada, S. Natarajan, J.J. Ródenas, H. Nguyen-Xuan, and S.P. Bordas, Computational Mechanics 52 (2013), pp. 37–52.

[57] O. González-Estrada, E. Nadal, J. Ródenas, P. Kerfriden, S.P.A. Bordas, and F. Fuenmayor, Computational Mechanics 53 (2014), pp. 957–976.

[58] S. Bordas and M. Duflot, Computer Methods in Applied Mechanics and Engineering 196 (2007), pp. 3381–3399.

[59] M. Duflot and S. Bordas, International Journal for Numerical Methods in Engineering 76 (2008), pp. 1123–1138.

[60] S. Bordas, M. Duflot, and P. Le, Communications in Numerical Methods in Engineering 24 (2008), pp. 961–971.